

Supplementary Material for **Phase transitions in a programmable quantum spin glass simulator**

R. Harris*, Y. Sato, A. J. Berkley, M. Reis, F. Altomare, M. H. Amin, K. Boothby, P. Bunyk, C. Deng, C. Enderud, S. Huang, E. Hoskinson, M. W. Johnson, E. Ladizinsky, N. Ladizinsky, T. Lanting, R. Li, T. Medina, R. Molavi, R. Neufeld, T. Oh, I. Pavlov, I. Perminov, G. Poulin-Lamarre, C. Rich, A. Smirnov, L. Swenson, N. Tsai, M. Volkmann, J. Whittaker, J. Yao

*Corresponding author. E-mail: rharris@dwavesys.com

Published 13 July 2018 as *Science* First Release
DOI: 10.1126/science.aat2025

This PDF file includes:

Materials and Methods
Figs. S1 to S15
Table S1
References

Other Supplementary Material for this manuscript includes the following: (available at www.sciencemag.org/content/361/6398/162/suppl/DC1)

Movie S1
Data Files as a separate .zip file

Materials and Methods

Flux qubit as Ising spin-1/2 particle

Fig. S1A depicts an Ising spin-1/2 particle in an external magnetic field. The application of a longitudinal magnetic field $B_{||}$ gives rise to Zeeman splitting between the up and down spin states of the particle, while the transverse magnetic field B_t gives rise to superposition states as shown in Fig. S1B. The physics of this so-called transverse field Ising spin (TFIS) can be described by the Hamiltonian $\hat{\mathcal{H}}_{\text{TFIS}} = -g\mu_B(B_{||}\hat{\sigma}_z + B_t\hat{\sigma}_x)$, where $\hat{\sigma}_z$ and $\hat{\sigma}_x$ are the Pauli z and x operators, μ_B is the Bohr magneton, and g is the particle's Landé g -factor.

A superconducting flux qubit can be used to represent a TFIS. Fig. S1C depicts a simplified schematic of a flux qubit (the kind often referred to as a CJJ rf SQUID), configured to allow for the application of magnetic flux to the two closed inductive loops. With the application of flux bias Φ_{cjj}^x to the smaller compound Josephson junction (CJJ) loop, two counter-circulating persistent current states $|\uparrow\rangle$ and $|\downarrow\rangle$ are induced, analogous to the up and down states of an Ising spin-1/2 particle. The potential energy landscape has two local minima, corresponding to these circulating current states, and the overall potential can be tilted by the application of flux bias Φ_q^x to the larger body loop. The 1D potential energy as a function of persistent current \hat{I}_q^p as well as the two lowest energy wavefunctions are shown in Fig. S1D. One can write an effective Hamiltonian as $\hat{\mathcal{H}}_q = -\frac{1}{2}(\epsilon\hat{\sigma}_z + \Delta\hat{\sigma}_x)$, where $\epsilon \propto |I_q^p|\Phi_q^x$ is the relative bias energy, $|I_q^p|$ acts as the effective magnetic moment of this 2-level system, and Δ represents the tunneling energy between the counter-circulating persistent current states. Comparing the two systems and their respective Hamiltonians, one sees that a flux qubit can be treated as an effective Ising spin-1/2 particle with ϵ (controlled by Φ_q^x) and Δ (controlled by Φ_{cjj}^x) playing the role of longitudinal and transverse magnetic fields, respectively. See (34) and references therein for a further description of flux qubits similar to those used in the experiments reported upon herein.

D-Wave quantum processing unit (QPU)

Many of the technical details of earlier generation QPUs have been previously published. The general description of the analog portion of the D-Wave One generation QPU architecture (14) still applies to the prototype used in this study. However, there are significant parametric differences between the analog devices found in these two generations, and the programming (35) and readout (36) infrastructure have been redesigned. Nonetheless, all D-Wave QPUs disclosed to date implement a transverse field Ising model (TFIM) of the form

$$\hat{\mathcal{H}}_{\text{DW}} = \mathcal{J}_{\text{AFM}}(s) \left[- \sum_{i=1}^N h_i \hat{\sigma}_i^z + \sum_{\langle i,j \rangle \in G} J_{ij} \hat{\sigma}_i^z \hat{\sigma}_j^z \right] - \frac{\Delta(s)}{2} \sum_{i=1}^N \hat{\sigma}_i^x, \quad (5)$$

where $\mathcal{J}_{\text{AFM}}(s)$ and $\Delta(s)$ are the problem and single qubit tunneling energy scales, respectively, h_i are dimensionless 1-local biases that can be applied to each individual qubit, and J_{ij} are dimensionless 2-local couplings between qubits i and j defined on the so-called Chimera graph G (35). The problem energy scale can be expressed in terms of device properties as $\mathcal{J}_{\text{AFM}}(s) \equiv M_{\text{AFM}} |I_q^p(s)|^2$, where M_{AFM} is the maximum allowed mutual inductance between a pair of flux qubits (37) and $|I_q^p(s)|$ is the s -dependent magnitude of the flux qubit persistent current (34).

An optical image of a single unit cell of the QPU is shown in Figs. S2A and B. The unit cell represents a $K_{4,4}$ bipartite graph containing a total of 8 physical qubits indexed by the numbers 0 to 7, as indicated in Fig. S2A. The flux qubits are arranged in two groups, one with their bodies stretched in the horizontal direction and the other with their bodies stretched in the vertical direction. An independently tunable inductive coupler is placed at each intersection of a horizontal and a vertical qubit body, as shown in Fig. S2B, thus giving rise to the $K_{4,4}$ bipartite connectivity. Additional couplers placed at both ends of each qubit provide couplings between adjacent unit cells when this structure is tiled on a square grid.

A complete QPU is composed of a 16×16 square array of the aforementioned unit cells, as shown in Fig. S2C. The QPU is cooled in a dilution refrigerator with base temperature $T_{\text{base}} \approx$

10 mK and interfaced with external controls via 192 cold low pass filtered differential current biases and a small number of high bandwidth single-ended coaxial lines for readout.

Lattice embedding

The Chimera graph was motivated by the desire to embed arbitrary logical graphs through the use of strong ferromagnetic (FM) bonds to define correlated sets of physical qubits. Doing so results in so-called logical qubits that possess higher connectivity than the individual physical qubits. The process of mapping a given logical Ising problem onto the Chimera graph is known as minor embedding, as described by Choi (38, 39). The simple cubic (SC) lattice embedding described herein is a particular minor embedding composed of a repeating pattern, as depicted in Fig. S3. Here, a set of 8 lattice spins are embedded in a 2×2 block of unit cells by FM linking chains of 4 physical qubits, as indicated by the colored bars. Couplers that bind members of a given spin, hereafter referred to as logical couplers, are depicted by solid black dots and are set to dimensionless coupling strength $J_{ij} = -2$. Couplers that are used to represent lattice couplings between spins are represented by solid white dots. Inter-unit cell couplers at the ends of horizontal physical qubits are used to embed the \hat{a} -axis couplings of the SC lattice and are set to $J_{ij} = \pm\alpha_a$, where $0 < \alpha_a < 1$. Inter-unit cell couplers at the ends of vertical physical qubits are likewise used to embed the \hat{b} -axis couplings of the SC lattice and are set to $J_{ij} = \pm\alpha_b$, where $0 < \alpha_b < 1$. \hat{c} -axis couplings are embedded in pairs of couplers at the intersections of the lattice spins. We draw attention to the existence of two distinct configurations of \hat{c} -axis couplings, as denoted by c_1 and c_2 in Fig. S3. Configuration c_1 couples pairs of physical qubits in the interior of the 4-long qubit chains, whereas configuration c_2 couples pairs of physical qubits at the ends of the 4-long qubit chains. This distinction has implications for programming of target Hamiltonians, as is discussed below. These couplers are set to $J_{ij} = \pm\alpha_{c1}/2$ or $\pm\alpha_{c2}/2$ for the c_1 and c_2 configurations, respectively. Tiling this 2×2 block on a square grid across the entire QPU completes the embedding of the $8 \times 8 \times 8$ SC lattice.

The SC lattice embedding used for the reported 3D lattice work is illustrated further in Fig. S4. For the sake of clarity, a $3 \times 3 \times 8$ lattice is used as an example. With the particular embedding scheme described above, a $3 \times 3 \times 8$ lattice requires 6×6 unit cells. Fig. S4A depicts a 6×6 unit cell section of the QPU, with each unit cell containing 4 horizontal and 4 vertical rectangles that represent physical qubits. Lattice couplings in the \hat{a} and \hat{b} -axis are shown in dark blue and those in the \hat{c} -axis are shown in light blue. Logical couplings that bind sets of four physical qubits are shown in black. Other couplers that are irrelevant for this specific minor embedding are not shown here for clarity. Figures S4A-D sequentially illustrate the process of edge contraction by merging the logical qubits together, thus revealing a 3D lattice. See the accompanying movie S1 for a more complete view of this process.

Physical qubit calibration

The QPU has been designed to provide *in situ* tunability of several key analog properties of the individual qubits and couplers. This complexity was motivated by the desire to homogenize analog device parameters in the presence of realistic fabrication variations. Lumped element models of all 2048 qubits and 6016 couplers are calibrated *in vivo* and the model parameters are subsequently homogenized to typically better than 3% maximum deviation.

A key summary of QPU calibration is a plot of the energy scales $\mathcal{J}_{\text{AFM}}(s)$ and $\Delta(s)$, hereafter referred to as the native Chimera annealing schedule, as shown in Fig. S5. The measured values of $\Delta(s)$, shown as solid points, were obtained by performing tunnel spectroscopy (40) on all 2048 qubits. These results were grouped according to qubit index in the unit cell (see Fig. S2 for the indexing) and plotted as the mean result for each index with error bars indicating the standard deviation of the distribution for that index. There is a well resolved parametric split by qubit index that has been attributed to a systematic variation in qubit capacitance on the order of 2 to 5 fF. The $\Delta(s)$ data indicate that there are 4 homologous pairs of qubit indices: (0,2), (1,3), (4,6), and (5,7).

To model the flux qubit properties, we found it sufficient to fit each of the spectroscopy data sets shown in Fig. S5 to a simplified rf SQUID Hamiltonian (34) of the form

$$\begin{aligned}\hat{\mathcal{H}}_{\text{rf}}(s) = & \frac{\hat{Q}_q^2}{2C_q} + \frac{\hat{Q}_{cjj}^2}{2C_{cjj}} - \frac{I_c\Phi_0}{\pi} \cos\left(\frac{\hat{\varphi}_{cjj}}{2}\right) \cos(\hat{\varphi}_q) \\ & + \frac{\Phi_0^2}{4\pi^2 L_q} \frac{(\hat{\varphi}_q - \varphi_q^x)^2}{2} + \frac{\Phi_0^2}{4\pi^2 L_{cjj}} \frac{(\hat{\varphi}_{cjj} - \varphi_{cjj}^x(s))^2}{2},\end{aligned}\quad (6)$$

where $\hat{\varphi}_q$ and \hat{Q}_q are the quantum mechanical phase and charge associated with the qubit body degree of freedom and $\hat{\varphi}_{cjj}$ and \hat{Q}_{cjj} are likewise the phase and charge associated with the compound Josephson junction (CJJ) degree of freedom. In both cases, the phase and charge obey the commutation relation $[\hat{\varphi}_{q(cjj)}, \hat{Q}_{q(cjj)}/2e] = i$, where e is the electron charge and $i = \sqrt{-1}$. See Fig. S6 for a mapping of the phases onto the device topology. This device is subjected to two external flux biases $\Phi_q^x \equiv \Phi_0\varphi_q^x/2\pi$ and $\Phi_{cjj}^x(s) \equiv \Phi_0\varphi_{cjj}^x(s)/2\pi$ that thread the qubit body and CJJ loops, respectively, as shown in Fig. S6. Note that the annealing parameter s -dependence is called out explicitly in the definition of $\Phi_{cjj}^x(s)$, thus imparting s -dependence to Hamiltonian 6 via $\varphi_{cjj}^x(s)$. The mapping from Φ_{cjj}^x to s is weakly nonlinear but nonetheless monotonic. The model is parameterized by the lumped element capacitances C_q and C_{cjj} , lumped element inductances L_q and L_{cjj} , and the single Josephson junction critical current I_c . For our devices, wherein $L_{cjj}/L_q \ll 1$, we have found it sufficient to take $L_{cjj} = 12 \text{ pH}$ and $C_{cjj} = 5 \text{ fF}$ from design. The parameters L_q and I_c are calibrated and homogenized *in vivo* using a series of persistent current measurements, thus leaving C_q as the only free parameter that needs to be inferred from fitting spectroscopy results. The mean calibrated lumped element model parameters (34) for the aforementioned 4 pairs of qubit indices are summarized in Table S1.

Figure S5 also summarizes the mean predicted problem energy scale $\mathcal{J}_{\text{AFM}}(s)$ obtained by coupling pairs of qubit models with the maximum allowed mutual inductance $M_{\text{AFM}} \equiv 2.15 \text{ pH}$ available on the particular QPU used in these experiments. The calculation involved solving for

the eigenstates of the following Hamiltonian:

$$\hat{\mathcal{H}}_{mn} = \hat{\mathcal{H}}_{\text{rfs},m} + \hat{\mathcal{H}}_{\text{rfs},n} + M_{\text{AFM}} \hat{I}_m^p(s) \hat{I}_n^p(s), \quad (7)$$

where $0 \leq m, n \leq 7$ indicate qubit position indices, $\mathcal{H}_{\text{rfs},m}$ is the isolated rf SQUID Hamiltonian 6 for a qubit with index m subject to $\Phi_0/2 < \Phi_{\text{cjj}}^x(s) < \Phi_0$ and $\Phi_q^x = 0$, and $\hat{I}_m^p(s) \equiv (\hat{\varphi}_q - \varphi_q^x)/L_q$ is the persistent current operator acting on qubit m as represented using the individual rf SQUID bases at annealing parameter s . The low energy eigenstates of Hamiltonian 7 can be mapped onto those of a coupled qubit Hamiltonian of the form

$$\hat{\mathcal{H}}_{2q} = -\frac{\Delta_m(s)}{2} \hat{\sigma}_m^x - \frac{\Delta_n(s)}{2} \hat{\sigma}_n^x + \mathcal{J}_{\text{AFM}}(s) \hat{\sigma}_m^z \hat{\sigma}_n^z. \quad (8)$$

Most notably, one can analytically solve for the eigenstates of Hamiltonian 8, which then reveals that the energy separation between the first and second excited states equals $2\mathcal{J}_{\text{AFM}}(s)$. The curve shown in Fig. S5 was obtained by performing the above calculation for all 24 possible pairwise couplings that exist in the Chimera graph, with 16 of those couplings located within a single unit cell and 8 couplings between unit cells, and averaging the results.

Coherence

The QPU used in this particular study was manufactured using the same fabrication process as that used in the entanglement study of Lanting *et al.* (41). In this previous work, the authors demonstrated the presence of equilibrium entanglement in a ferromagnetically coupled 8-qubit ring via a combination of spectroscopic and occupation probability measurements. The relevance of the entanglement study in the context of the work reported upon herein is twofold: First, the experimental spectroscopy results alone indicate that this physical system provides a faithful implementation of the TFIM, at least at the scale of a single unit cell. Second, the demonstration of equilibrium entanglement, which is thermodynamically stable, indicates that the embedded TFIM Hamiltonian is not an ephemeral condition that breaks down within a finite coherence time. In this regard, the QPU used for this work is similar to solid state systems that

are described by the TFIM (11, 12) in that the Hamiltonian is realized in the laboratory frame of reference and weak coupling to a thermal environment leads to thermal occupation of the energy eigenstates of the TFIM. This is in contrast to other physical implementations of programmable quantum simulators wherein the TFIM is realized in a rotating frame of reference and decoherence causes the state of the system to leave the TFIM energy eigenbasis (2–9).

While the results of Lanting *et al.* are encouraging, they nonetheless leave two unanswered questions: First, under what conditions is the assumption of weak (perturbative) coupling between the QPU and the thermal environment justified? Second, how can one seek signs of quantum behavior at scales beyond a single unit cell of the QPU? The former question can be answered using an average model of decoherence for the QPU while the latter question is key motivation for this particular manuscript.

Much of the technical language pertaining to decoherence in the context of qubits and quantum computing has been borrowed from the field of nuclear magnetic resonance (NMR). In what follows, we will refer to two particular NMR timescales: The relaxation time T_1 that characterizes the timescale over which an ensemble of magnetic moments initialized in an excited energy eigenstate relax to their equilibrium configuration by exchanging energy with their environment; and the pure dephasing time T_φ that characterizes the timescale over which an ensemble of magnetic moments initialized into a non-stationary state dephase in the absence of T_1 relaxation. These two timescales appear as components of the aggregate decoherence time T_2 via the relation $1/T_2 = 1/2T_1 + 1/T_\varphi$. Assuming ergodicity, these timescales for a single measurement of an ensemble of magnetic moments can be used to describe the statistical evolution of a single qubit over an ensemble of measurements.

We begin by characterizing T_1 in our flux qubits and discussing its importance in the context of quantum annealing. Let the environment seen by a single qubit be described by a set of modes λ , for each of which there is a noise spectral density $S_\lambda(\omega)$ that is a function of an-

gular frequency ω . Assuming weak coupling between a qubit and its environment, T_1 can be expressed in terms of upward and downward transition rates, γ_- and γ_+ , respectively, that are calculated via Fermi's golden rule:

$$\frac{1}{T_1} \equiv \frac{1}{\gamma_+} + \frac{1}{\gamma_-}; \quad (9)$$

$$\frac{1}{\gamma_\pm} = \frac{1}{\hbar^2} \sum_{\lambda} S_{\lambda}(\pm\Omega) \left| \langle g | \hat{\mathcal{O}}_{\lambda} | e \rangle \right|^2 \delta[\hbar|\Omega| - (E_e - E_g)]. \quad (10)$$

Here, Ω represents an angular frequency, E_g and E_e are the ground state $|g\rangle$ and first excited state $|e\rangle$ energy of the qubit, respectively, and $\hat{\mathcal{O}}_{\lambda}$ is an operator coupling the qubit to environmental mode λ . Similar to the analysis of Yan *et al.* (42), we have determined that our flux qubits are coupled to a combination of charge and flux noise. Here, charge noise can be predominantly attributed to dielectric loss in amorphous SiO_x around the qubit wiring, with dielectric loss tangent $\tan \delta \approx 3 \times 10^{-3}$. This gives rise to a charge noise spectral density

$$S_Q(\omega) \equiv \int_{-\infty}^{+\infty} dt e^{i\omega t} \langle \hat{Q}_x(t) \hat{Q}_x(0) \rangle = 2\hbar C_q \tan \delta \frac{\text{sign}(\omega)}{1 - \exp(-\hbar\omega/k_B T)} \quad (11)$$

that couples to the flux qubit via the substitution $\hat{Q}_{\text{q}} \rightarrow \hat{Q}_{\text{q}} - \hat{Q}_x(t)$ in Hamiltonian 6, where $\hat{Q}_x(t)$ represents the time-dependent charge noise operator. Flux noise in our devices can be characterized as a sum of two components: First, there is a $1/f$ -like component $S_{\Phi}^{\text{lf}}(\omega)$ of amplitude $2\mu\Phi_0/\sqrt{\text{Hz}}$ at $\omega/2\pi = 1\text{ Hz}$ and exponent $\alpha \approx 0.8$. This low frequency component can be written as

$$S_{\Phi}^{\text{lf}}(\omega) \equiv \int_{-\infty}^{+\infty} dt e^{i\omega t} \langle \hat{\Phi}_x^{\text{lf}}(t) \hat{\Phi}_x^{\text{lf}}(0) \rangle \approx \frac{A^2}{(\omega/2\pi)^{\alpha}}, \quad (12)$$

where the approximation indicates that this symmetric about $\omega = 0$ form is only valid in the low frequency limit $\hbar|\omega| \ll k_B T$. Second, there is a broad Ohmic component that can be parameterized by an effective shunt resistance $R_s \approx 80\text{ k}\Omega$:

$$S_{\Phi}^{\text{hf}}(\omega) \equiv \int_{-\infty}^{+\infty} dt e^{i\omega t} \langle \hat{\Phi}_x^{\text{hf}}(t) \hat{\Phi}_x^{\text{hf}}(0) \rangle = \frac{2L_q^2}{R_s} \frac{\hbar\omega}{1 - \exp(-\hbar\omega/k_B T)}. \quad (13)$$

The environmental flux mode operators couple to the flux qubit via the substitution $\hat{\varphi}_q - \varphi_q^x \rightarrow \hat{\varphi}_q - \varphi_q^x - 2\pi\hat{\Phi}_x^{\text{lf}}(t)/\Phi_0 - 2\pi\hat{\Phi}_x^{\text{hf}}(t)/\Phi_0$ in Hamiltonian 6, where $\hat{\Phi}_x^{\text{lf}}(t)$ and $\hat{\Phi}_x^{\text{hf}}(t)$ represent time-dependent flux noise operators. Using the physical qubit parameters listed in Table S1 and temperature $T = 12\text{ mK}$, we obtain the summary of T_1 versus s for an average physical qubit at degeneracy $E_e - E_g = \Delta$ shown in Fig. S7. Note that $T_1 \lesssim 10\text{ ns}$ for $s \lesssim 0.5$, which is the range of s that is relevant for the experiments reported upon herein, and that it is dominated by flux noise for all s .

Given the above calculation of T_1 , one can now determine over what range of s the coupling to the environment can be characterized as weak. The calculation of T_1 described above is valid in the limit $\mathcal{Q} \equiv \Omega T_1 \gg 1$, where \mathcal{Q} can be interpreted as a physical qubit quality factor. Figure S7 also shows the results of a calculation of \mathcal{Q} versus s for an average physical qubit at degeneracy $E_e - E_g = \Delta(s)$. For $\mathcal{Q} \gg 1$, the physics of the open quantum system can be approximately modeled by first order perturbation theory. We identify the region $s \lesssim 0.37$ as being characterized by weak coupling to the environment. For $\mathcal{Q} \gtrsim 1$, increasingly higher orders of perturbation theory are required to accurately model the qubit's physics with increasing s . In this regime, roughly for $0.37 \lesssim s \lesssim 0.55$, which can be characterized by intermediate coupling to the environment, the qubit's excitation energy will be renormalized and an excitation will decay in a time faster than T_1 . For $\mathcal{Q} \lesssim 1$, the qubit is strongly coupled to the environment and the dynamics of the qubit are characterized by incoherent tunneling between a pair of localized states.

Within the context of the experiments reported upon herein, the key observation to be taken from Fig. S7 is that all of the observed phase transitions occur at $s < 0.23$, which is well within the weak coupling regime. Furthermore, this plot underlines one of the key principles in the practical design of QA processors: One must choose global device parameters to ensure that phase transitions, such as those shown in this study, occur within the weak coupling regime.

Reductions in dissipative noise will allow the weak coupling regime to expand to higher s , which can then impact QA processor performance.

We now turn to the topic of the dephasing processes that give rise to T_φ . Noise spectral density at angular frequencies $|\omega_{\text{lf}}| < |\omega| < |\omega_{\text{hf}}| \ll E_e - E_g$ contribute to dephasing. Here, ω_{lf} is a low frequency cutoff that is inversely related to the time between successive applications of active compensation for environmentally induced drift in qubit properties, which was typically on the scale of minutes, and ω_{hf} is a high frequency cutoff that is inversely proportional to the single shot measurement time, which typically ranged from 1 ms to 1 s. Environmental fluctuations over the range $|\omega_{\text{hf}}| < |\omega| < E_e - E_g$ give rise to fast oscillations that are averaged out over the course of a single shot measurement whereas those at frequencies $|\omega| < |\omega_{\text{lf}}|$ appear as static offsets that can be measured and compensated. Integrating a noise spectral density over the appropriate frequency range gives the observable amplitude of the mean squared fluctuations for a particular environmental operator. For our devices, the low frequency fluctuations are dominated by the aforementioned $1/f$ -like flux noise, for which we estimate the root mean squared (rms) amplitude to be

$$\delta\Phi_{\text{lf}}^{\text{rms}} = \sqrt{\left\langle \hat{\Phi}_{\text{lf}}^2(t) \right\rangle} = \left[2 \int_{\omega_{\text{lf}}}^{\omega_{\text{hf}}} d\omega S_\Phi(\omega) \right]^{1/2} \approx 8 \mu\Phi_0 , \quad (14)$$

where we have integrated only over positive ω and multiplied that result by 2 under the assumption that $S(\omega) \approx S(-\omega)$ for $\hbar\omega_{\text{lf}} < \hbar\omega_{\text{hf}} \ll k_B T$. Substituting $\hat{\varphi}_q - \varphi_q^x \rightarrow \hat{\varphi}_q - \varphi_q^x - \delta\Phi_{\text{lf}}^{\text{rms}}$ in Hamiltonian 6 gives rise to a bias energy $\delta\epsilon_{\text{rms}}$ that must then be compared to the desired inter-qubit coupling energy, as given by the quantity $\mathcal{J}_{\text{AFM}}(s)$ shown in Fig. S5 multiplied by a constant factor between 0.1 and 2, depending on the details of a given particular experiment. Figure S8 shows \mathcal{J}_{AFM} and $\delta\epsilon_{\text{rms}}$ versus s , where we have multiplied the latter quantity by 30 in order to make it visible on the same vertical axis scale. Given that $\mathcal{J}_{\text{AFM}}(s) \gg \delta\epsilon_{\text{rms}}$ for the range of s that is relevant for our experiments, we are confident that the perturbations to

the target coupled qubit Hamiltonian 5 via low frequency flux noise are weak. Nonetheless, this analysis makes it clear that the physics that gives rise to dephasing in superconducting gate model quantum computing hardware is also important in the context of QA in that low frequency fluctuations impact the precision to which target Hamiltonians can be specified. Reductions in low frequency noise will allow one to more accurately specify target Hamiltonians with smaller coupling energies, which then impacts QA processor performance.

We now return to the question of how does one probe quantum mechanical behavior in large scale QA processors. It should be noted that the study of Lanting *et al.* (41) was restricted to probing entanglement within a single unit cell simply due to the details of how bias lines were arranged in the processor. Given that inter-qubit couplers are nearly parametrically identical within and between unit cells, there is no reason to expect that a coupled 8-qubit system that spanned multiple unit cells would behave any different. However, we do anticipate the tunnel spectroscopy method used by Lanting *et al.* will not be a viable way forward to probe quantum behavior at the scale of an entire 2048-qubit QA processor. This situation is very much akin to that in the gate model quantum computing community, wherein full state tomography is the workhorse method for demonstrating quantum behavior of small prototype systems but is viewed as being impractical on large scale systems. Our work in this manuscript represents a completely different approach to addressing this question: Using methods that are appropriate for condensed matter systems composed of a thermodynamically large number of degrees of freedom, ask whether a large scale QA processor can reproduce known theoretical results from the field of quantum magnetism.

Lattice spin model

Since the SC lattice is an embedded problem, the single physical qubit annealing schedule shown in Fig. S5 must be replaced by similar graph that is appropriate for the 4-long chains of physical qubits that represent the lattice spins. This was accomplished by using the mean calibrated physical qubit models to predict the eigenspectra of isolated and coupled lattice spins.

To calculate the transverse field splitting $\Gamma(s)$, we implemented quantum mechanical models of isolated 4-long physical qubit chains composed of qubit indices 0-0-4-4 (or equivalently 2-2-6-6) and 1-1-5-5 (or equivalently 3-3-7-7). See Figs. S2 and S3 for the indices and chain configurations, respectively. Each physical qubit was represented by an rf SQUID model given by Hamiltonian 6, from which a basis of up to 8 eigenstates was obtained. The 4-long chain eigenstates were then calculated using a set of up to 8^4 basis states:

$$\hat{\mathcal{H}}_{\text{chain}}(s) = \sum_{n=1}^4 \hat{\mathcal{H}}_{\text{rfs},n}(s) + \sum_{n=1}^3 J_{\text{logical}} M_{\text{AFM}} \hat{I}_n^p \hat{I}_{n+1}^p, \quad (15)$$

where the first term is the sum of the isolated rf SQUID Hamiltonians given in Hamiltonian 6 and the second term embodies the linear couplings between the rf SQUIDs via a mutual inductance $J_{\text{logical}} M_{\text{AFM}}$, with $J_{\text{logical}} = -2$ for these experiments, and the product of the rf SQUID persistent current operators, as represented using the individual rf SQUID bases at annealing parameter s . The results of these calculations as a function of annealing parameter s are shown in Fig. S9. Note that this particular embedding of the SC lattice results in nearly identical eigenspectra versus s for the two types of chains. Most important, there is a clear separation into a low and high energy manifold for $s \gtrsim 0.15$. We identify the two lowest lying states as the TFIM spin-1/2 states and their energy spacing as the transverse field splitting $2\Gamma(s)$.

To calculate the coupling energy $\mathcal{J}(s)$, one must carefully consider each of the coupling configurations between lattice spins. Couplings in the \hat{a} - and \hat{b} -axis directions are implemented between a physical qubit at one end of a first 4-long chain and a middle qubit in a second 4-

long chain. The two \hat{c} -axis configurations, denoted as c_1 and c_2 , have been described above. A schematic representation of these coupling configurations is depicted in Fig. S10. We implemented models of each of these 3 distinct coupling configurations by first calculating a set of 8 basis states for each 4-long chain in isolation, as described above, and then solving for the eigenstates of the coupled pair of chains using the set of 8^2 basis states:

$$\hat{\mathcal{H}}_{\text{2chain}} = \hat{\mathcal{H}}_{\text{chain},1}(s) + \hat{\mathcal{H}}_{\text{chain},2}(s) + \overleftrightarrow{M} \cdot \overleftrightarrow{I}_{\text{chain},1}^p \cdot \overleftrightarrow{I}_{\text{chain},2}^p, \quad (16)$$

where the first two terms are the isolated chain Hamiltonians of the form Hamiltonian 15, \overleftrightarrow{M} is a 4×4 tensor representing the inductive couplings of the individual rf SQUIDs between the chains, and $\overleftrightarrow{I}_{\text{chain},1(2)}^p$ is a tensor representation of the rf SQUID persistent current operators as represented within the basis defined by the eigenstates of an isolated chain. The entries to \overleftrightarrow{M} for couplings in the \hat{a} - or \hat{b} -axis directions are all 0 except for a single entry that is set to $\pm \alpha_i M_{\text{AFM}}$, where $i \in [a, b]$ and $0 < |\alpha_i| < 1$ are dimensionless parameters that can be used to independently adjust the magnitude of the coupling strength along each crystal axis. Similarly, the entries to \overleftrightarrow{M} for couplings in the \hat{c} -axis direction are all 0 except for two entries that are both set to $\pm \alpha_i M_{\text{AFM}}/2$ for $i \in [c1, c2]$.

It should be noted that the technique described above of first calculating the physical properties of individual isolated chains and then solving for the eigenstates of a pair of chains was validated by comparing to the results of a much more computationally intensive calculation starting from the basis formed from the lowest 4 eigenstates of 8 individual rf SQUIDs at a few representative values of s . It was observed that the results were identical to within a few percent, thus lending confidence to the former, and much faster, procedure.

A comparison of the coupled chain eigenspectra versus s for uniform isotropic dimensionless coupling strength $\alpha_a = \alpha_b = \alpha_{c1} = \alpha_{c2} = 0.3$ is shown in Fig. S11A. For each configuration, the four lowest lying states can be identified as being those of coupled TFIM spin-1/2

particles. The low energy physics of this system was then mapped onto the eigenstates of the following simplified Hamiltonian:

$$\hat{\mathcal{H}}_{2q} = -\Gamma(s)\hat{\sigma}_1^x - \Gamma(s)\hat{\sigma}_2^x + \mathcal{J}(s)\hat{\sigma}_1^z\hat{\sigma}_2^z, \quad (17)$$

for which an analytic calculation reveals that the energy spacing between the first and second excited state equals $2\mathcal{J}$. While the results for the \hat{a} - and \hat{b} -axis couplings are identical, it is evident that the two \hat{c} -axis coupling configurations yield significantly different results. This discrepancy can be attributed to the imperfect correlation of the 4 qubits within a given chain at relatively low s . In particular, the c_2 configuration yields the smallest $\mathcal{J}(s)$ while the c_1 configuration yields the largest $\mathcal{J}(s)$. Repeating these calculations for isotropic $0.2 \leq \alpha \leq 0.8$ revealed that the values of $\mathcal{J}(s)$ for the c_1 and c_2 configurations differ from those obtained in either the \hat{a} or \hat{b} configuration by a factor of 1.4 and 0.71, respectively, over the narrow range of s that is relevant for these experiments. As an explicit demonstration, coupled chain eigenspectra versus s for corrected dimensionless coupling strengths $\alpha_a = \alpha_b = 0.3$, $\alpha_{c1} = 0.3/1.4$, and $\alpha_{c2} = 0.3/0.71$ are shown in Fig. S11B. To within an accuracy of a few percent, these corrections to the magnitudes of the \hat{c} -axis couplings homogenize the eigenspectra and therefore the inferred values of $\mathcal{J}(s)$.

The nearest neighbor spin-spin correlation $\langle s_i s_j \rangle$ provides an effective way to check the efficacy of these corrections and the model that predicts them. Here a spin state s_i is defined to take a value of either +1 or -1, and i and j denote the nearest neighbor site locations. The expectation value of the product of the two neighboring spin states can be measured for every neighboring combination of spins. In the AFM phase with $p = 0$, the spins are highly correlated and the nearest neighbor spin-spin correlation is -1 throughout the lattice, which makes the evaluation of coupling strength variations within the lattice nontrivial. Instead, one can carry out the measurement in the PM phase before the system becomes fully correlated to probe

systematic coupling strength variations within the lattice. See Fig. S11C for the histogram of $\langle s_i s_j \rangle$ for all nearest neighbor Ising spin combinations with $\alpha_a = \alpha_b = \alpha_{c1} = \alpha_{c2} = 0.3$ and $p = 0$ at $s = 0.1$. The data are grouped by bond type. It is clear that results for the a -axis and b -axis couplings are equal while the c_1 and c_2 configurations lead to the strongest and weakest couplings, which is consistent with the predictions from the spectral analysis. See Fig. S11D for the data taken with $\alpha_a = \alpha_b = 0.3$, $\alpha_{c1} = 0.3/1.41$ and $\alpha_{c2} = 0.3/0.71$, which demonstrates that the corrected couplings result in homogenized spin-spin correlation statistics.

A summary of the calculated energy scales $\Gamma(s)$ and mean $\mathcal{J}(s)$ for $\alpha_a = \alpha_b = 0.3$, $\alpha_{c1} = 0.3/1.4$, and $\alpha_{c2} = 0.3/0.71$ is shown in Fig. S12, from which one can readily obtain the scaled transverse field $\Gamma(s)/\mathcal{J}(s)$. This curve then provides a unique mapping from the annealing parameter s to Γ/\mathcal{J} . This mapping has been used to translate the linear susceptibility peak positions s_c in Figs. 2D and 2E into Γ/\mathcal{J} , as shown in Fig. 4.

Experimental protocols

All of the measurements presented herein were collected using one of two modified forms of the quantum annealing algorithm, as depicted in Fig. S13. These pseudo-waveforms depict a common protocol for manipulating the transverse magnetic field via the time-dependence of $s(t)$ but differing protocols for probing the longitudinal magnetic field response via an independently controlled global time-dependent flux signal $\Phi_{||}^x(t)$ that is applied to every physical qubit.

For both order parameter and susceptibility measurements, the system was initialized in the PM phase at $s = 0$, slowly annealed to an intermediate target value of $0 < s < 1$ followed by a long pause to allow for equilibration, and then a fast quench to $s = 1$. The anneal and pause times were varied between typical values on the order of 1 ms for examining AFM instances ($p < p_c = 0.22$) to 100 ms for examining SG instances ($p > p_c$). Measurements were repeated on small sets of instances as a function of anneal and pause time to ensure equilibration to within

experimental precision. The quench time varied linearly with the target annealing parameter as $(1-s) \times (100 \text{ ns})$ for target $0 < s < 1$. Note that the quench times were relatively long compared to both the single physical qubit tunneling rates $h/\Delta(s)$ and the lattice spin tunneling rates $h/2\Gamma(s)$ over the range of s that was relevant for these experiments. As such, we would have been unable to perform projective measurements of either isolated physical qubits or isolated lattice spins using this protocol. However, large lattices of coupled spins exhibit dynamical slowing (43, 44) upon approaching a phase transition, thus allowing one to faithfully measure the magnetization statistics of such a lattice near the phase boundary in the PM phase and throughout the AFM and SG phases.

The experimental results shown in Figs. 2A-C and 3 were collected using the order parameter protocol depicted in Fig. S13A. In this case, the longitudinal field $\Phi_{||}^x(t) = 0$, thus there is no intentional symmetry breaking.

The experimental results shown in Fig. 2D-F were collected using the susceptibility protocol depicted in Fig. S13B. Here, the system is annealed in zero longitudinal field to the target value of s , and then a small longitudinal magnetic field is applied, which was realized by applying a magnetic flux of amplitude $< 3\mu\Phi_0$ to every physical qubit on the QPU, during the pause in $s(t)$. The sign of the longitudinal field was toggled between two subsequent measurement frames and the difference in the magnetic state of the lattice was recorded, thus providing an approximate measurement of the linear susceptibility.

The $p - s$ phase diagram from spin-spin overlap analysis

Whereas Hartmann used the variance of $|q|$ to distinguish the spin-glass and ferromagnetic phase (15), one can use a qualitatively similar quantity $\int_{-2\sigma}^{2\sigma} P(q)dq$ to differentiate the SG, AFM, and PM phases. Choosing σ to be the standard deviation associated with the Gaussian $P(q)$ in the PM phase for each disorder p , we see that this spin-spin overlap integral approaches 1 and 0 in the PM and AFM phases, respectively, and a finite value indicative of a nontrivial

energy landscape in the SG phase. Figure S14 shows the measured integral versus s and p . This constitutes an effective phase diagram for this system, and it shows a sharp PM to AFM transition and much broader PM to SG transition, consistent with the linear susceptibility measurements. A summary of s_c from linear susceptibility peak positions and p_c^{exp} from Binder cumulant analysis are also shown for reference.

The $\Gamma/\mathcal{J} - k_B T/\mathcal{J}$ phase diagram for $p = 0$

Assuming that the lattice is in thermal equilibrium, sweeping the quantum annealing parameter s results in a curved trajectory in a 2-dimensional space defined by scaled temperature $k_B T/\mathcal{J}(s)$ and scaled transverse field $\Gamma(s)/\mathcal{J}(s)$. The calibrated qubit electronic temperature for these experiments was $T = 12.0 \pm 0.1$ mK. Using this temperature and the energy scales $\Gamma(s)$ and $\mathcal{J}(s)$ depicted in Fig. S12, quantum annealing with this system maps out the gray manifold depicted in Fig. 1A. Note that any such annealing manifold for $T > 0$ intersects the AFM and SG phase boundaries at transverse fields that are guaranteed to be less than the values obtained in the limit $T \rightarrow 0$. Thus, the projected phase diagram shown in Fig. 4A is in qualitative agreement with the expected outcome.

As an additional crosscheck on the scaled temperature and scaled transverse field calibration, we measured the AFM susceptibility χ_{AFM} as a function of s for the pure AFM instance ($p = 0$) for multiple dimensionless coupling strengths defined by $(\alpha_a, \alpha_b, \alpha_{c1}, \alpha_{c2}) \equiv \alpha \times (0.3, 0.3, 0.3/1.4, 0.3/0.71)$. Doing so scales $\mathcal{J}(s)$, thus altering the annealing trajectory in $(\Gamma/\mathcal{J}, k_B T/\mathcal{J})$ -space. The measurements of χ_{AFM} versus s are shown in Fig. S15. The trajectories for a sample of values of $0.33 < \alpha < 2.67$ are shown as dashed curves in Fig. 4B. The positions of the peaks in $\chi_{\text{AFM}}(s)$ versus s were then converted to points on those trajectories, with the error bars indicating the uncertainty in the peak position along each trajectory.

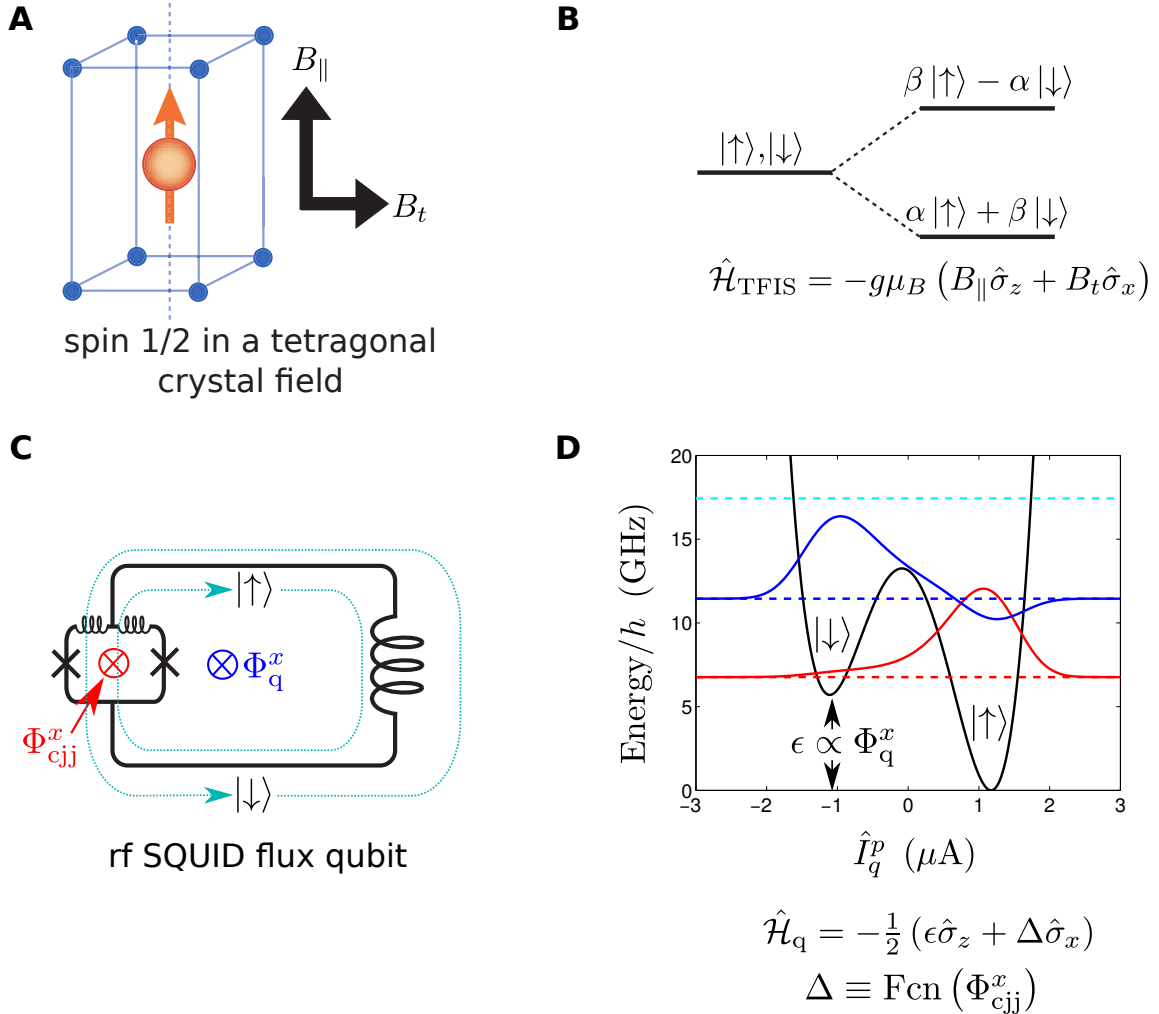


Fig. S1. Mapping of the TFIM onto a flux qubit. (A) An Ising spin-1/2 subject to an external magnetic field with longitudinal B_{\parallel} and transverse B_t field components. Such a system can be realized by placing the spin-1/2 within a potential possessing tetragonal symmetry. (B) Level diagram for the Ising spin-1/2. B_{\parallel} breaks inversion symmetry, thus giving rise to Zeeman splitting between the spin states $|\uparrow\rangle$ and $|\downarrow\rangle$. B_t does not break inversion symmetry, rather it lifts degeneracy by giving rise to superposition states $(|\uparrow\rangle \pm |\downarrow\rangle)/\sqrt{2}$. An arbitrarily oriented external magnetic field gives rise to a combination of Zeeman splitting and superposition, as given by the eigenstates of the Hamiltonian $\hat{\mathcal{H}}_{\text{TFIM}}$. (C) A simplified circuit diagram of a compound Josephson junction (CJJ) rf SQUID flux qubit subject to externally controlled flux biases Φ_q^x and Φ_{cjj}^x . The low energy physics of this system can be described by two counter-circulating persistent current states, $|\uparrow\rangle$ (clockwise) and $|\downarrow\rangle$ (counter-clockwise). (D) Low energy eigenstates of the CJJ rf SQUID Hamiltonian. Graph depicts the potential energy landscape (solid black curve) and the two lowest energy wavefunctions (solid red and blue curves). The low energy physics of this device is captured by the flux qubit Hamiltonian $\hat{\mathcal{H}}_q$.

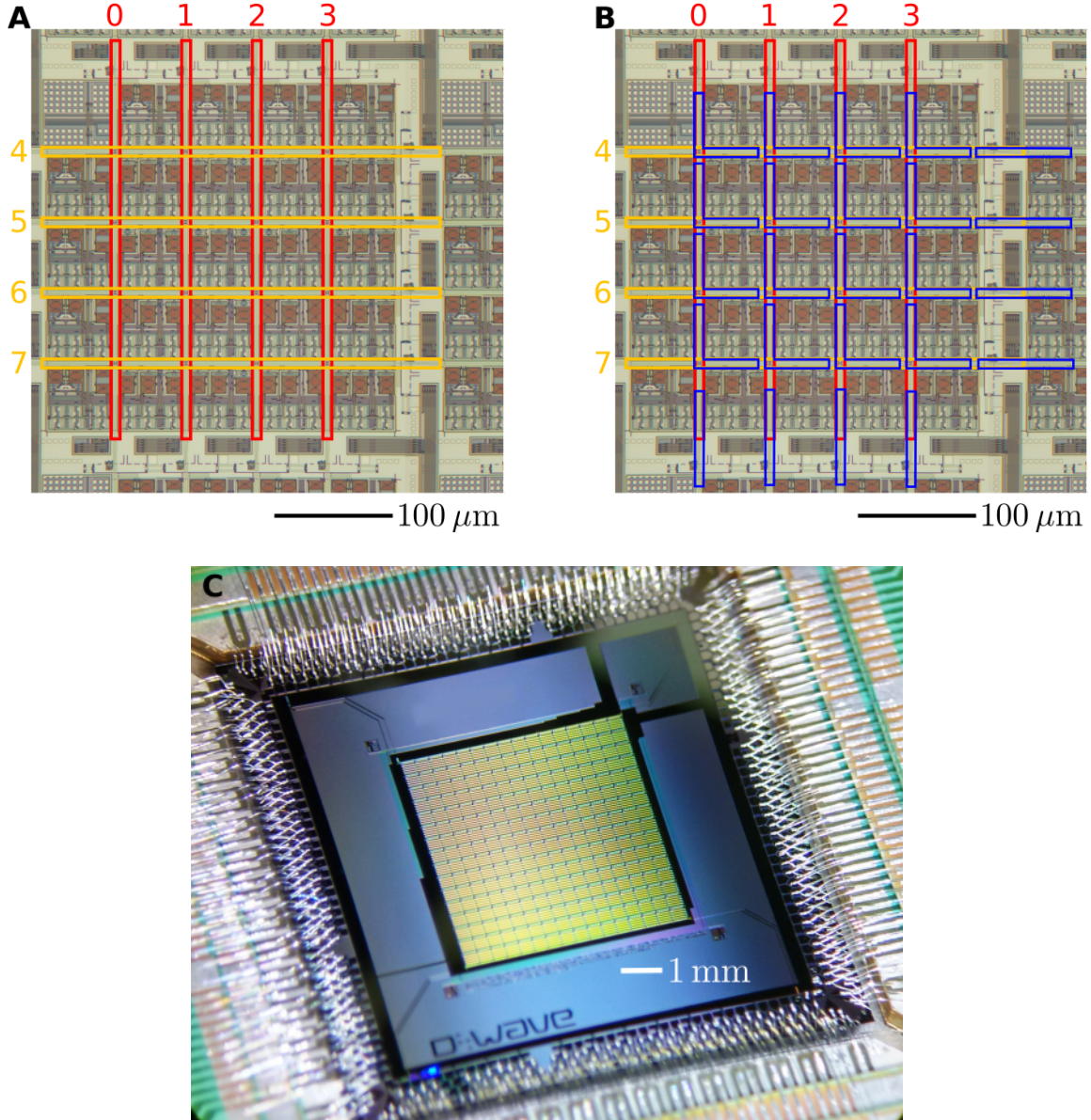


Fig. S2. QPU unit cell topology. (A) Optical image of a unit cell with physical qubit bodies annotated as closed loops (device details omitted for clarity). Vertical and horizontal qubits are shown in red and gold, respectively. Qubit positions are indexed by the numbers 0 to 7 inclusive. (B) Coupler bodies, annotated as blue loops (device details omitted for clarity) overlay each intersection of a horizontal and vertical qubit pair. The result is a $K_{4,4}$ bipartite graph. Additional coupler bodies at the ends of the qubits connect to qubits in neighboring unit cells when this entire structure is tiled on a square grid. (C) Optical image of a complete QPU. The circuit contains a 16×16 array of unit cells.

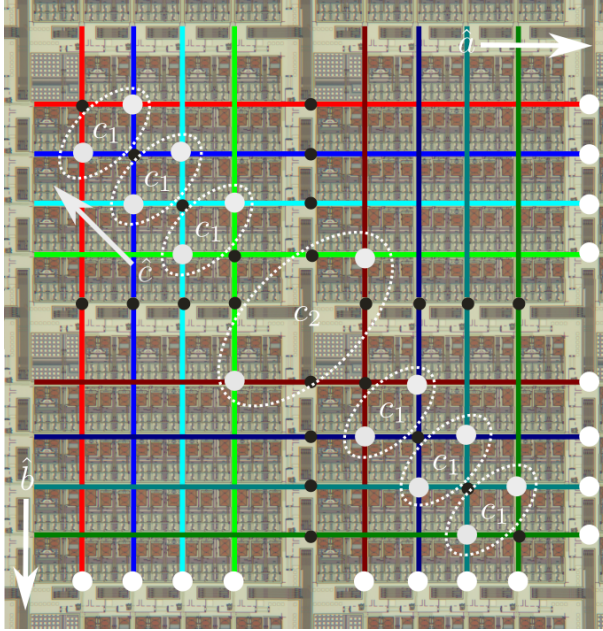


Fig. S3. Minor embedding of the 3-dimensional cubic lattice on the Chimera graph. The optical image depicts a 2×2 block of unit cells. Lattice spins are embedded in 4-long chains of physical qubits, which are represented by sets of like-colored bars, that are bound together by strong ferromagnetic couplings, as indicated by solid black dots. Each 2×2 block of unit cells contains 8 such lattice spins. Couplers along the right and bottom sides of the block are used to embed \hat{a} -axis and \hat{b} -axis couplings, respectively, as denoted by solid white dots, when this entire structure is tiled on a square grid. \hat{c} -axis couplings are embedded in pairs of couplers where pairs of lattice sites intersect, as indicated by solid white dots within dashed white ellipses. These latter couplings come in two configurations: c_1 wherein the two inner physical qubits of each chain are coupled; and c_2 wherein the two physical qubits at the ends of each chain are coupled.

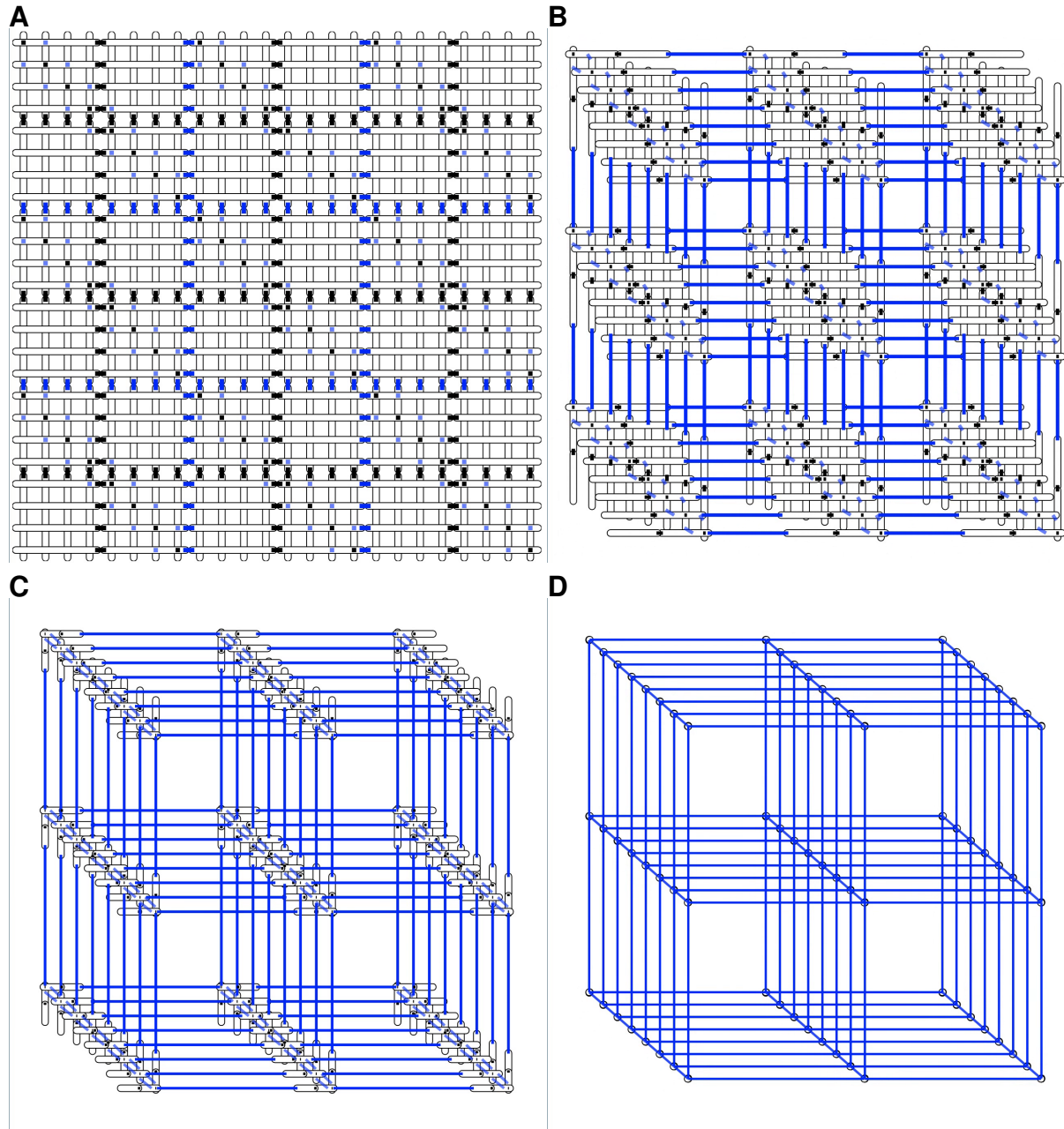


Fig. S4. Illustration of 3D lattice embedding using a $3 \times 3 \times 8$ example. In (A), 6×6 unit cells are shown with horizontal and vertical rectangles representing physical qubits. Logical couplers that bind the 4-qubit chains are shown as black dots. a and b couplers are shown in dark blue whereas c couplers are shown in light blue. (A)-(D) sequentially merge those qubits bound by logical couplers, revealing a $3 \times 3 \times 8$ lattice.

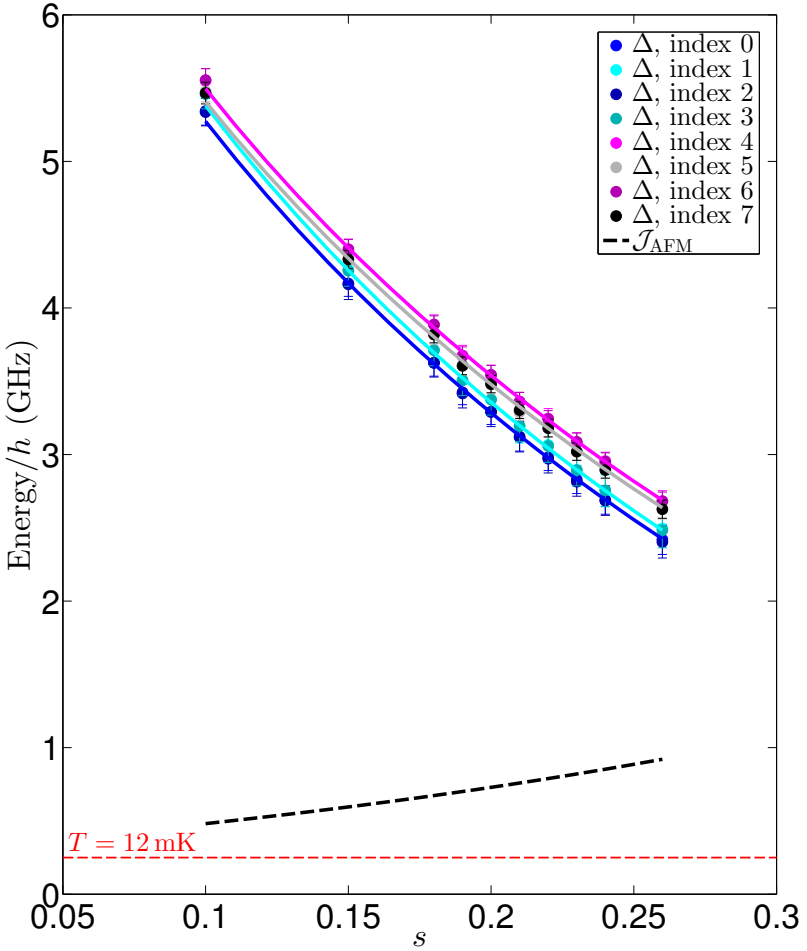


Fig. S5. Summary of physical qubit spectroscopy measurements across the entire 2048-qubit QPU, and mean predicted physical qubit coupling energy versus s . Solid points represent tunneling energies for each index averaged over all unit cells within the QPU. The data indicate that $\Delta(s)$ systematically varies between qubit positions, with the index pairs (0,2), (1,3), (4,6), and (5,7) corresponding to parametrically different devices. The solid curves are best fits to lumped element device models wherein the qubit body capacitance was the only free parameter. The dashed curve represents the predicted mean coupling energy averaged over all possible pairwise couplings of physical qubits on the Chimera graph.

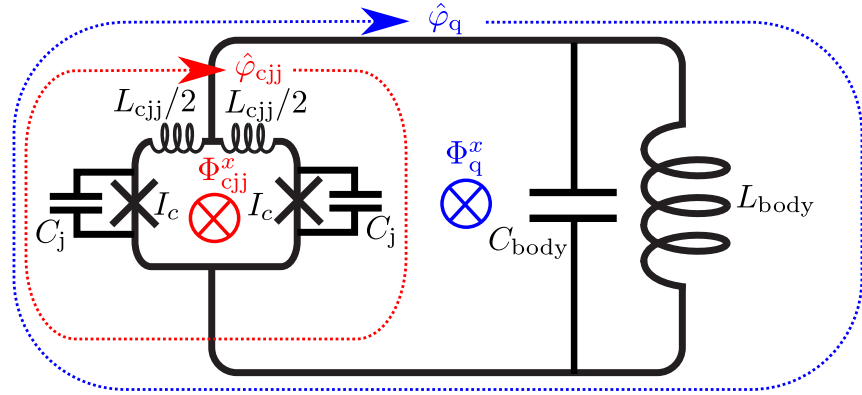


Fig. S6. Compound Josephson junction (CJJ) flux qubit topology. The device is composed of two closed inductive loops of superconducting metal, as indicated by solid black curves. The properties of the body loop can be represented by a lumped element model consisting of an inductance L_{body} and a capacitance C_{body} . This loop is subjected to a flux bias Φ_q^x and currents that flow about this loop are governed by a phase $\hat{\varphi}_q$. The CJJ loop possesses an inductance L_{cjj} that is symmetrically divided between its two branches, and a single Josephson junction of critical current I_c and capacitance C_j interrupts each branch. This loop is subjected to an external flux bias Φ_{cjj}^x and currents that flow about this loop are governed by a phase $\hat{\varphi}_{\text{cjj}}$. The q mode is parameterized by the lumped element parameters $L_q \equiv L_{\text{body}} + L_{\text{cjj}}/4$ and $C_q \equiv C_{\text{body}} + 2C_j$. The cjj mode is parameterized by the lumped element parameters L_{cjj} and $C_{\text{cjj}} \equiv C_j/2$.

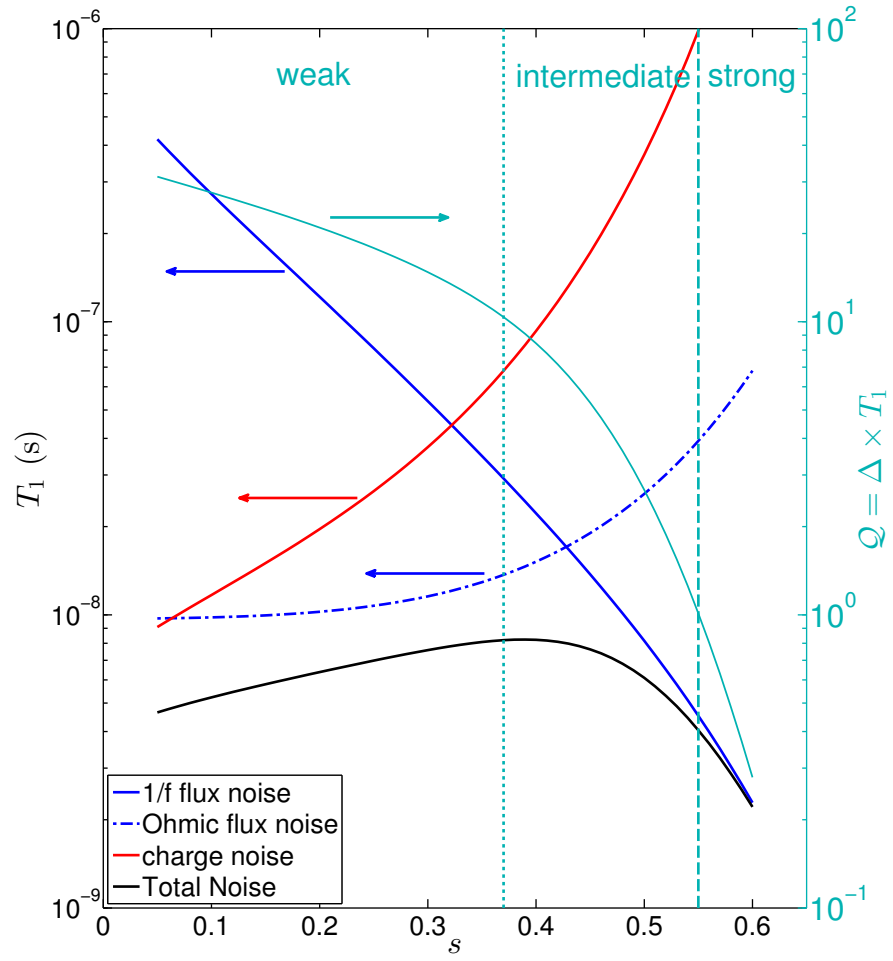


Fig. S7. Average model of relaxation timescale T_1 versus s . Left vertical axis: T_1 due to individual mechanisms and the sum of all mechanisms. Right axis: Physical qubit quality factor defined by the product of the energy splitting $\Delta(s)$ multiplied by T_1 . Horizontal arrows indicate the corresponding vertical axis for each trace. Crossovers between the weak, intermediate, and strong coupling regimes roughly indicated by dashed vertical lines.

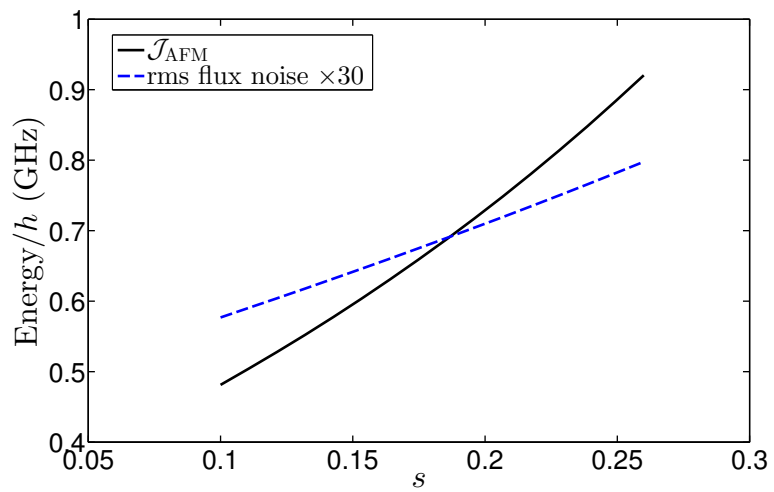


Fig. S8. Root mean squared flux noise versus s. Comparison of the reference inter-qubit coupling energy $\mathcal{J}_{\text{AFM}}(s)$ to the rms flux noise multiplied by 30.

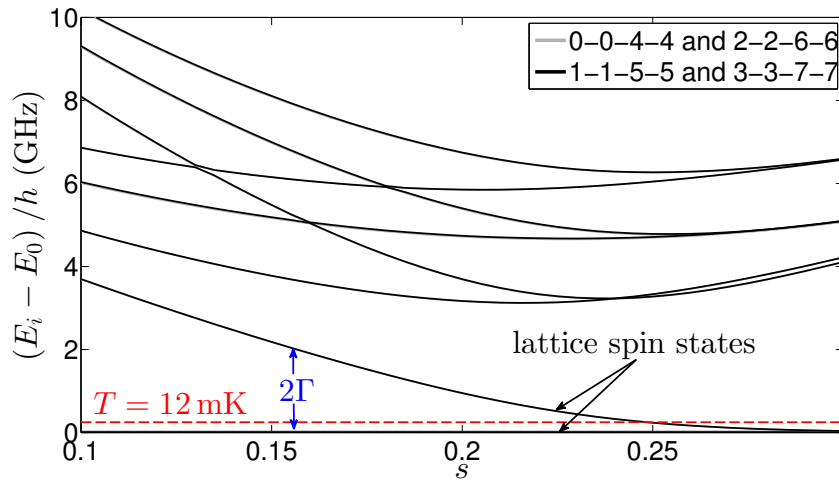


Fig. S9. Calculated eigenspectra versus quantum annealing parameter s for two configurations of 4-qubit chains. The eigenspectra are very close to being identical to within the resolution of this plot. The two lowest energy states can be mapped onto those of a TFIM spin-1/2 with energy splitting 2Γ .

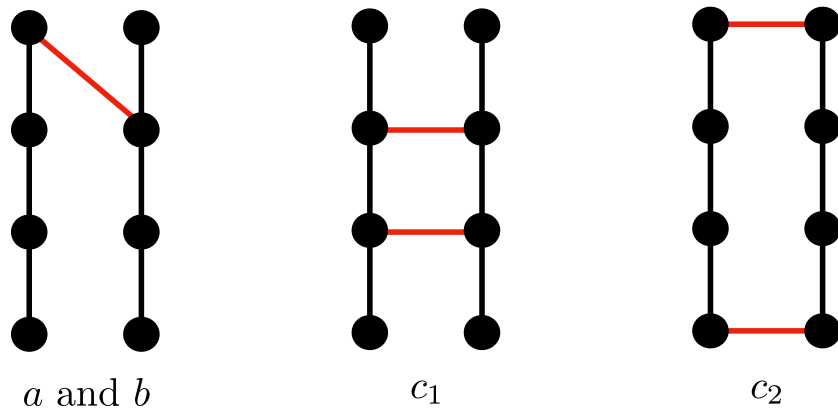


Fig. S10. Schematic representation of three distinct configurations used for coupling 4-qubit chains. Physical qubits correspond to solid black dots. Strong ferromagnetic couplings used to define the chains are indicated by solid black lines. Each 4-qubit chain forms an effective Ising spin. Lattice couplings between chains are indicated by solid red lines. From left to right, the configurations are for coupling two effective Ising spins in a and b -axis, c_1 -axis, and c_2 -axis.

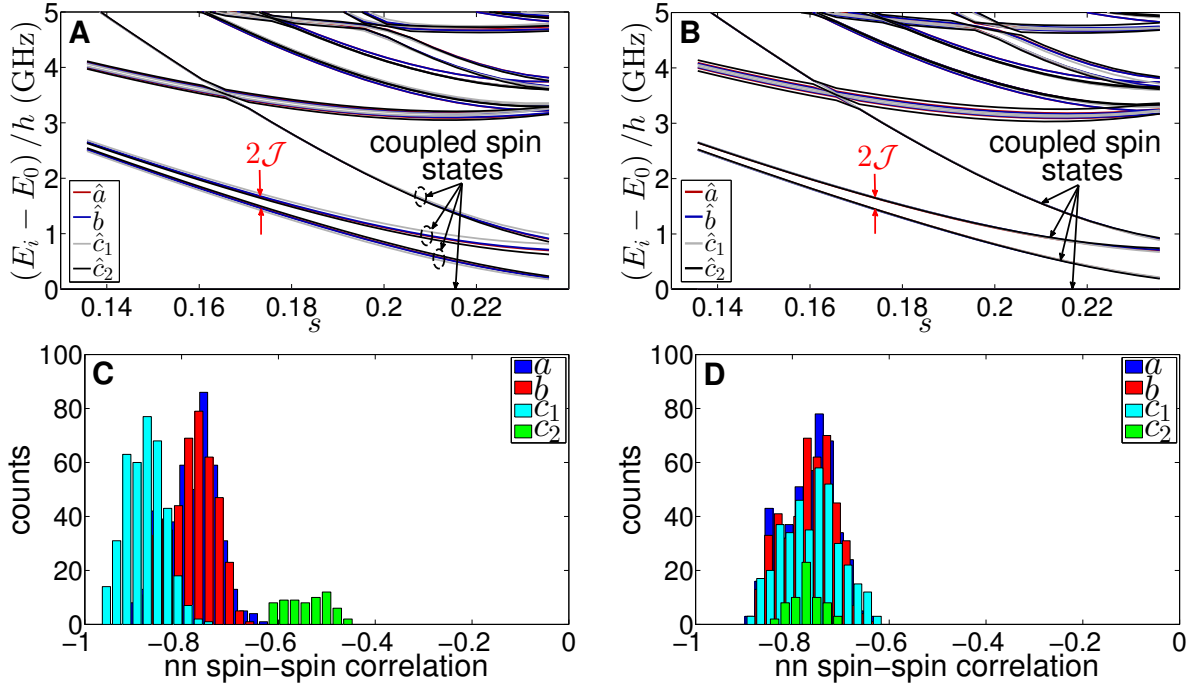


Fig. S11. Calculated eigenspectra versus quantum annealing parameter s for pairs of coupled 4-qubit chains. (A) Calculated eigenspectra versus s for the 4 lattice coupling configurations for uniform dimensionless coupling strength $\alpha_a = \alpha_b = \alpha_{c1} = \alpha_{c2} = 0.3$. The energy spacing between the first and second excited states equals $2\mathcal{J}(s)$ for a coupled pair of 2-level systems. Note the discrepancies between the eigenspectra, with coupling configuration $c_1(c_2)$ yielding the largest (smallest) $\mathcal{J}(s)$. (B) As in (A), but for adjusted dimensionless coupling strengths $\alpha_a = \alpha_b = 0.3$, $\alpha_{c1} = 0.3/1.4$, and $\alpha_{c2} = 0.3/0.71$. Note that the lowest four energies are nearly indistinguishable between the eigenspectra for $s \lesssim 0.22$. (C) Measured nearest neighbor spin-spin correlation histograms obtained by annealing the pure AFM ($p = 0$) instance to target $s = 0.1$. The results indicate anisotropy, with the highest and lowest correlations occurring in the \hat{c} -axis direction. The correlation statistics are split based on coupling configuration. (D) as in (C), but for the adjusted coupling strengths. Note that the correlations are isotropic.

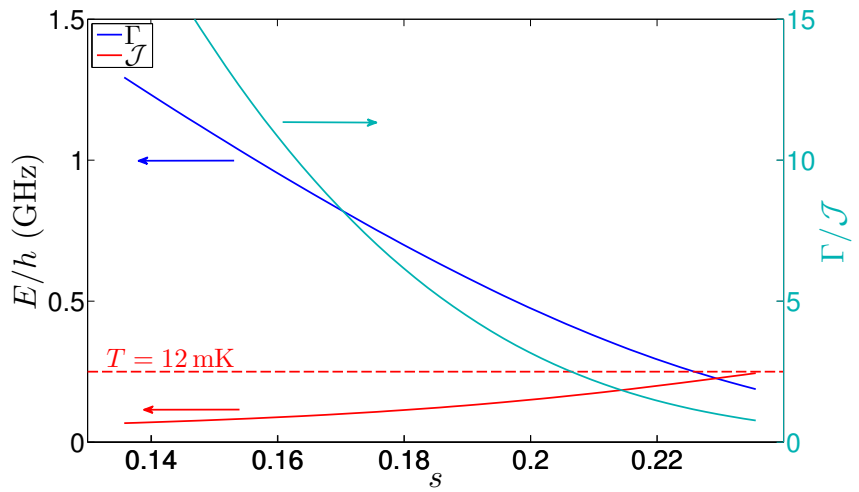


Fig. S12. Predicted scaled transverse field Γ/\mathcal{J} versus s . Left axis: Energy, corresponding to either Γ or \mathcal{J} , in units of frequency. Right axis: Dimensionless transverse field Γ/\mathcal{J} . Horizontal arrows indicate the corresponding vertical axis for each trace. Results are for dimensionless lattice coupling strengths $\alpha_a = \alpha_b = 0.3$, $\alpha_{c1} = 0.3/1.4$, and $\alpha_{c2} = 0.3/0.71$. $\Gamma(s)$ was obtained by averaging the predictions shown in Fig. S9 for the two chain configurations. $\mathcal{J}(s)$ was obtained from a weighted average of the energy spacing between the first and second excited states shown in Fig. S11B.

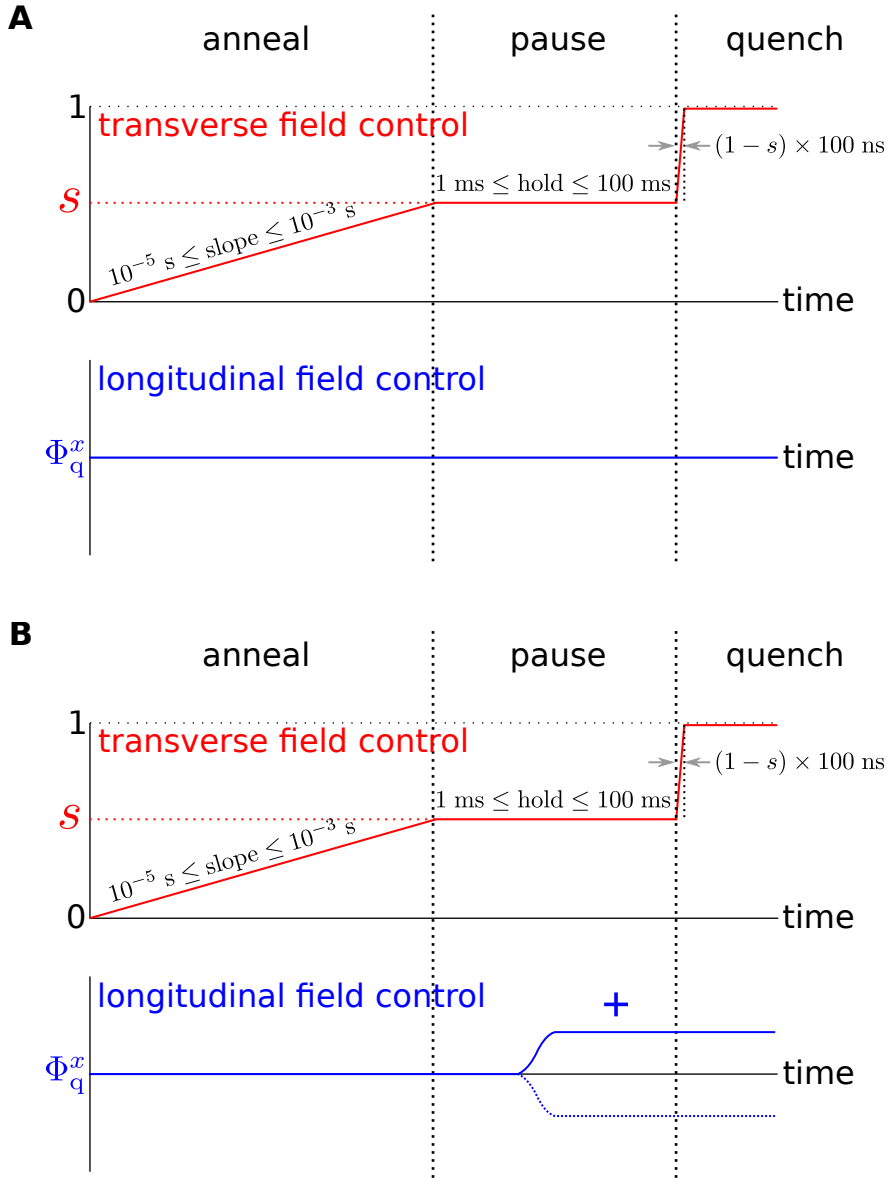


Fig. S13. Experimental protocols. (A) Pseudo-waveform sequence for measuring order parameters. The transverse field splitting $\Gamma(s)$ is a monotonic function of the annealing parameter $0 \leq s \leq 1$, with $\Gamma(s = 0) \gg \Gamma(s = 1)$. The sequence begins with a slow anneal from $s = 0$ to some intermediate target value of s , a long hold at the target s , and then a rapid quench to $s = 1$ in a time $(1 - s) \times 100 \text{ ns}$. The longitudinal field, which is linearly proportional to a global flux bias applied to all flux qubit bodies, is held at zero throughout. (B) Pseudo-waveform sequence for measuring susceptibility. The transverse field sequence is identical in form to that in (A), but in this case a small longitudinal field is slowly applied in the hold region. Toggling the sign of the longitudinal field between two measurement frames and recording the change in the state of the lattice yields a measurement of the susceptibility.

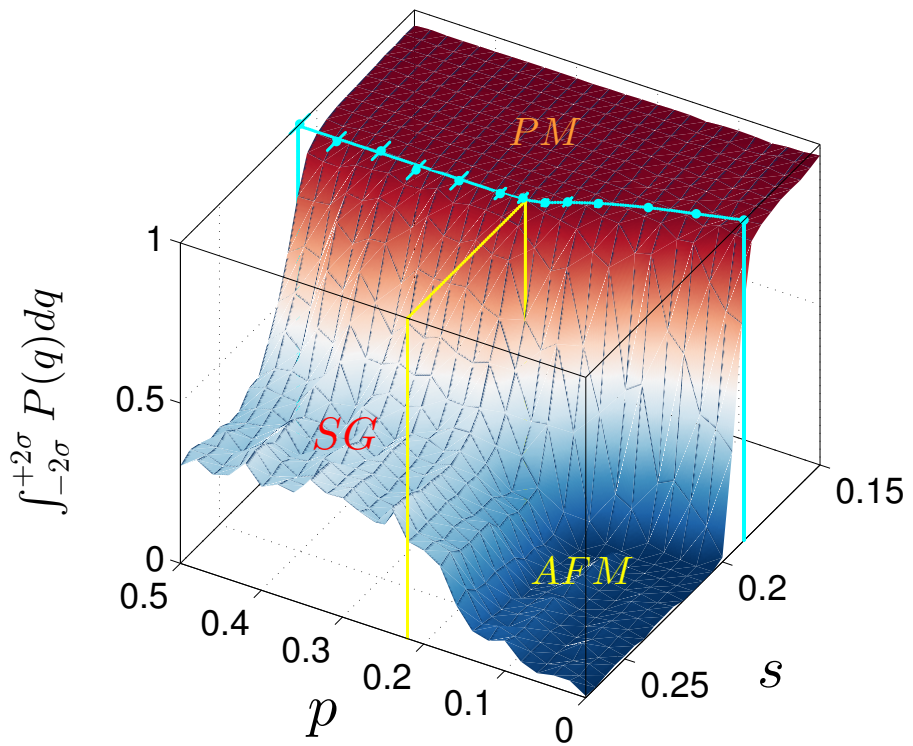


Fig. S14. **p – s phase diagram inferred from integrated spin-spin overlap.** Peak positions from linear susceptibility measurements are also shown (cyan) as well as the critical p_c^{exp} (yellow).

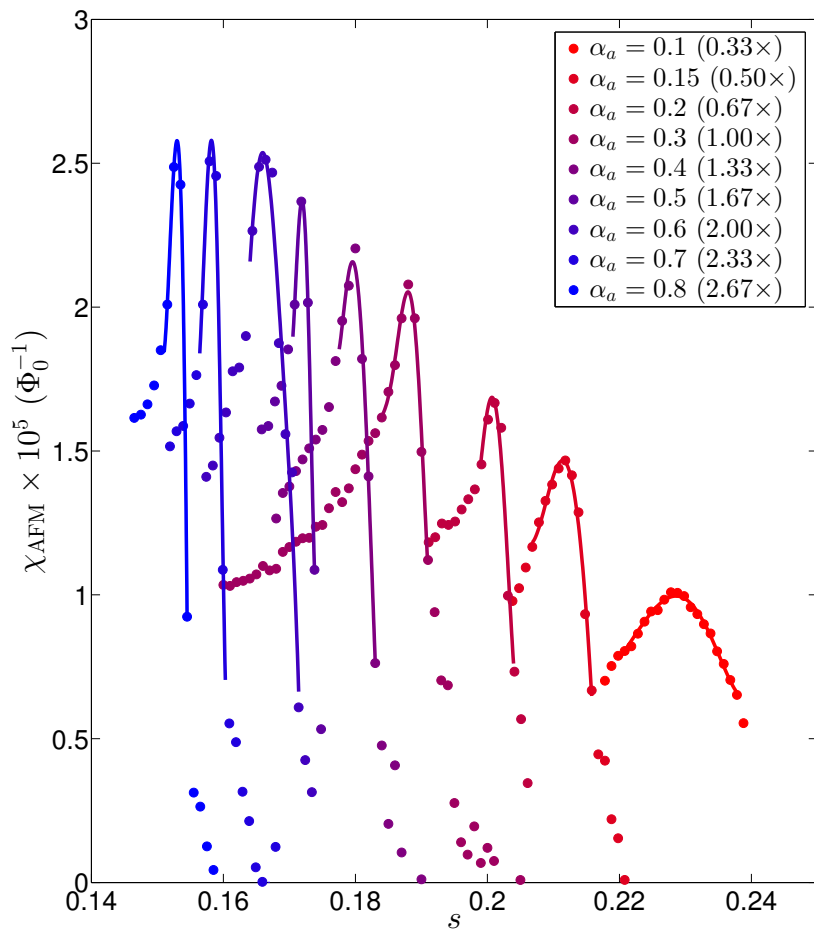


Fig. S15. Measurements of the AFM susceptibility χ_{AFM} versus s for varying dimensionless coupling strength α_a . Note that the peak position moves to lower s with increasing α_a .

| Indices | L_q (pH) | C_q (fF) | I_c (μ A) |
|---------|------------|------------|------------------|
| 0,2 | 298 | 121 | 2.48 |
| 1,3 | 298 | 115 | 2.48 |
| 4,6 | 283 | 122 | 2.45 |
| 5,7 | 283 | 127 | 2.45 |

Table S1: Summary of flux qubit lumped element model parameters for the 4 homologous pairs of qubit indices.

Movie S1: Illustration of 3D lattice embedding using a $3 \times 3 \times 8$ example. A 6×6 block of unit cells are shown with horizontal and vertical rectangles representing physical qubits. Lattice couplings in the \hat{a} and \hat{b} -axis are shown in dark blue and those in the \hat{c} -axis are shown in light blue. Logical couplings that bind sets of four physical qubits are shown in black. Other couplers that are irrelevant for this specific embedding are not shown here for clarity. As the movie progresses, logical qubits are merged together, and an effective three-dimensional lattice is shown. See the Supplementary Materials for more details.

Description of Data Files

The compressed data archive provided with this manuscript contains the following list of files in comma-separated values (csv) format. All columns are labeled and the units on each quantity are documented in the header of each file.

- critical-disorder-analysis-L=x.csv, where $x \in \{4, 6, 8\}$. These files contain the mean absolute magnetization $|m|_{\text{AFM}}$ and Binder cumulant g versus disorder p for each system size $L = x$ that are shown in Figs. 2A and 2B of the main text.
- chi-vs-s-p=x-alpha=0.3.csv, where $x \in \{0.0, 0.05, 0.1, 0.15, 0.18, 0.2, 0.225, 0.25, 0.3, 0.35, 0.4, 0.45, 0.5\}$. These files contain the susceptibility χ_{AFM} versus annealing parameter s that are shown in Figs. 2D and 2E in the main text. Note that the traces for $x = 0.18$ and $x = 0.225$ were omitted from those plots for the sake of clarity.
- overlap-distributions-p=x.csv, where $x \in \{0.1, 0.5\}$. These files contain count versus q , which can be easily converted to probability $P(q)$ versus q , for each of the 4 traces shown in Figs. 3A and 3B in the main text.
- physical-qubit-spectroscopy.csv. This file contains the mean spectral gap $\Delta(s)$ versus annealing parameter s for each of the 8 qubit indices in the processor unit cell, as shown in Fig. S5 in the Supplementary Materials.
- int-pqdq-vs-p-vs-s.csv. This file contains the integral of the spin-spin overlap distribution $\int_{-2\sigma}^{+2\sigma} P(q) dq$ versus disorder p and annealing parameter s , as shown in Fig. S14 in the Supplementary Materials.
- chi-vs-s-p=0.0-alpha=y.csv, where $y \in \{0.0, 0.1, 0.2, 0.3, 0.4, 0.5, 0.6, 0.7, 0.8\}$. These files contain the susceptibility χ_{AFM} versus annealing parameter s that are shown in Fig. S15 in the Supplementary Materials.

References and Notes

1. R. P. Feynman, Simulating physics with computers. *Int. J. Theor. Phys.* **21**, 467–488 (1982). [doi:10.1007/BF02650179](https://doi.org/10.1007/BF02650179)
2. C. Gross, I. Bloch, Quantum simulations with ultracold atoms in optical lattices. *Science* **357**, 995–1001 (2017). [doi:10.1126/science.aal3837](https://doi.org/10.1126/science.aal3837) Medline
3. H. Weimer, M. Müller, I. Lesanovsky, P. Zoller, H. P. Büchler, A Rydberg quantum simulator. *Nat. Phys.* **6**, 382–388 (2010). [doi:10.1038/nphys1614](https://doi.org/10.1038/nphys1614)
4. H. Bernien, S. Schwartz, A. Keesling, H. Levine, A. Omran, H. Pichler, S. Choi, A. S. Zibrov, M. Endres, M. Greiner, V. Vuletić, M. D. Lukin, Probing many-body dynamics on a 51-atom quantum simulator. *Nature* **551**, 579–584 (2017). [doi:10.1038/nature24622](https://doi.org/10.1038/nature24622) Medline
5. J. Zhang, G. Pagano, P. W. Hess, A. Kyprianidis, P. Becker, H. Kaplan, A. V. Gorshkov, Z.-X. Gong, C. Monroe, Observation of a many-body dynamical phase transition with a 53-qubit quantum simulator. *Nature* **551**, 601–604 (2017). [doi:10.1038/nature24654](https://doi.org/10.1038/nature24654) Medline
6. A. Friedenauer, H. Schmitz, J. T. Glueckert, D. Porras, T. Schaetz, Simulating a quantum magnet with trapped ions. *Nat. Phys.* **4**, 757–761 (2008). [doi:10.1038/nphys1032](https://doi.org/10.1038/nphys1032)
7. K. Kim, M.-S. Chang, S. Korenblit, R. Islam, E. E. Edwards, J. K. Freericks, G.-D. Lin, L.-M. Duan, C. Monroe, Quantum simulation of frustrated Ising spins with trapped ions. *Nature* **465**, 590–593 (2010). [doi:10.1038/nature09071](https://doi.org/10.1038/nature09071) Medline
8. X. Ma, B. Dakic, W. Naylor, A. Zeilinger, P. Walther, Quantum simulation of the wavefunction to probe frustrated Heisenberg spin systems. *Nat. Phys.* **7**, 399–405 (2011). [doi:10.1038/nphys1919](https://doi.org/10.1038/nphys1919)
9. J. Zhang, M.-H. Yung, R. Laflamme, A. Aspuru-Guzik, J. Baugh, Digital quantum simulation of the statistical mechanics of a frustrated magnet. *Nat. Commun.* **3**, 880 (2012). [doi:10.1038/ncomms1860](https://doi.org/10.1038/ncomms1860) Medline
10. S. Suzuki, J.-I. Inoue, B. K. Chakrabarti, *Quantum Ising Phases and Transitions in Transverse Ising Models* (Springer, 2012).
11. R. Blinc, B. Žekš, J. F. Sampaio, A. S. T. Pires, F. C. S. Barreto, Ising model in a transverse tunneling field and proton-lattice interaction in H-bonded ferroelectrics. *Phys. Rev. B* **20**, 1991–2001 (1979). [doi:10.1103/PhysRevB.20.1991](https://doi.org/10.1103/PhysRevB.20.1991)
12. W. Wu, B. Ellman, T. F. Rosenbaum, G. Aeppli, D. H. Reich, From classical to quantum glass. *Phys. Rev. Lett.* **67**, 2076–2079 (1991). [doi:10.1103/PhysRevLett.67.2076](https://doi.org/10.1103/PhysRevLett.67.2076) Medline
13. M. Suzuki, ed., *Quantum Monte Carlo Methods* (Springer, 1986).
14. R. Harris, M. W. Johnson, T. Lanting, A. J. Berkley, J. Johansson, P. Bunyk, E. Tolkacheva, E. Ladizinsky, N. Ladizinsky, T. Oh, F. Cioata, I. Perminov, P. Spear, C. Enderud, C. Rich, S. Uchaikin, M. C. Thom, E. M. Chapple, J. Wang, B. Wilson, M. H. S. Amin, N. Dickson, K. Karimi, B. Macready, C. J. S. Truncik, G. Rose, Experimental investigation of an eight-qubit unit cell in a superconducting optimization processor. *Phys. Rev. B* **82**, 024511 (2010). [doi:10.1103/PhysRevB.82.024511](https://doi.org/10.1103/PhysRevB.82.024511)
15. A. K. Hartmann, Ground-state behavior of the three-dimensional $\pm J$ random-bond Ising model. *Phys. Rev. B* **59**, 3617–3623 (1999). [doi:10.1103/PhysRevB.59.3617](https://doi.org/10.1103/PhysRevB.59.3617)

16. C. Domb, M. Green, eds., *Phase Transitions and Critical Phenomena* (Academic, 1974).
17. R. N. Bhatt, A. P. Young, Search for a transition in the three-dimensional J Ising spin-glass. *Phys. Rev. Lett.* **54**, 924–927 (1985). [doi:10.1103/PhysRevLett.54.924](https://doi.org/10.1103/PhysRevLett.54.924) [Medline](#)
18. R. M. Stratt, Path-integral methods for treating quantal behavior in solids: Mean-field theory and the effects of fluctuations. *Phys. Rev. B Condens. Matter* **33**, 1921–1930 (1986). [doi:10.1103/PhysRevB.33.1921](https://doi.org/10.1103/PhysRevB.33.1921) [Medline](#)
19. R. R. P. Singh, A. P. Young, Efficient generation of series expansions for $\pm J$ Ising spin glasses in a classical or a quantum field. *Phys. Rev. B* **96**, 214210 (2017). [doi:10.1103/PhysRevB.96.214210](https://doi.org/10.1103/PhysRevB.96.214210)
20. T. Kadowaki, H. Nishimori, Quantum annealing in the transverse Ising model. *Phys. Rev. E Stat. Phys. Plasmas Fluids Relat. Interdiscip. Topics* **58**, 5355–5363 (1998). [doi:10.1103/PhysRevE.58.5355](https://doi.org/10.1103/PhysRevE.58.5355)
21. E. Farhi, J. Goldstone, S. Gutmann, J. Lapan, A. Lundgren, D. Preda, A quantum adiabatic evolution algorithm applied to random instances of an NP-complete problem. *Science* **292**, 472–475 (2001). [doi:10.1126/science.1057726](https://doi.org/10.1126/science.1057726) [Medline](#)
22. J. Brooke, D. Bitko, T. F. Rosenbaum, G. Aeppli, Quantum annealing of a disordered magnet. *Science* **284**, 779–781 (1999). [doi:10.1126/science.284.5415.779](https://doi.org/10.1126/science.284.5415.779) [Medline](#)
23. V. Privman, ed., *Finite Size Scaling and Numerical Simulations of Statistical Systems* (World Scientific, 1990).
24. K. Binder, Finite size scaling analysis of Ising model block distribution functions. *Z. Phys. B Condens. Matter* **43**, 119–140 (1981). [doi:10.1007/BF01293604](https://doi.org/10.1007/BF01293604)
25. H. G. Katzgraber, F. Hamze, R. S. Andrist, Glassy chimeras could be blind to quantum speedup: Designing better benchmarks for quantum annealing machines. *Phys. Rev. X* **4**, 021008 (2014). [doi:10.1103/PhysRevX.4.021008](https://doi.org/10.1103/PhysRevX.4.021008)
26. M. Guo, R. N. Bhatt, D. A. Huse, Quantum critical behavior of a three-dimensional Ising spin glass in a transverse magnetic field. *Phys. Rev. Lett.* **72**, 4137–4140 (1994). [doi:10.1103/PhysRevLett.72.4137](https://doi.org/10.1103/PhysRevLett.72.4137) [Medline](#)
27. S. F. Edwards, P. W. Anderson, Theory of spin glasses. *J. Phys. F Met. Phys.* **5**, 965–974 (1975). [doi:10.1088/0305-4608/5/5/017](https://doi.org/10.1088/0305-4608/5/5/017)
28. H. Nishimori, *Statistical Physics of Spin Glasses and Information Processing: An Introduction* (Oxford Science Publications, 2001).
29. M. Hasenbusch, A. Pelissetto, E. Vicari, Critical behavior of three-dimensional Ising spin glass models. *Phys. Rev. B* **78**, 214205 (2008). [doi:10.1103/PhysRevB.78.214205](https://doi.org/10.1103/PhysRevB.78.214205)
30. R. J. Elliott, C. Wood, The Ising model with a transverse field. I. High temperature expansion. *J. Phys. C Solid State Phys.* **4**, 2359–2369 (1971). [doi:10.1088/0022-3719/4/15/023](https://doi.org/10.1088/0022-3719/4/15/023)
31. Y. L. Loh, D. X. Yao, E. W. Carlson, Thermodynamics of Ising spins on the triangular kagome lattice: Exact analytical method and monte carlo simulations. *Phys. Rev. B* **77**, 134402 (2008). [doi:10.1103/PhysRevB.77.134402](https://doi.org/10.1103/PhysRevB.77.134402)

32. R. Moessner, S. L. Sondhi, P. Chandra, Two-dimensional periodic frustrated ising models in a transverse field. *Phys. Rev. Lett.* **84**, 4457–4460 (2000).
[doi:10.1103/PhysRevLett.84.4457](https://doi.org/10.1103/PhysRevLett.84.4457) [Medline](#)
33. G. Misguich, D. Serban, V. Pasquier, Quantum dimer model on the kagome lattice: Solvable dimer-liquid and ising gauge theory. *Phys. Rev. Lett.* **89**, 137202 (2002).
[doi:10.1103/PhysRevLett.89.137202](https://doi.org/10.1103/PhysRevLett.89.137202) [Medline](#)
34. R. Harris, J. Johansson, A. J. Berkley, M. W. Johnson, T. Lanting, S. Han, P. Bunyk, E. Ladizinsky, T. Oh, I. Perminov, E. Tolkacheva, S. Uchaikin, E. M. Chapple, C. Enderud, C. Rich, M. Thom, J. Wang, B. Wilson, G. Rose, Experimental demonstration of a robust and scalable flux qubit. *Phys. Rev. B* **81**, 134510 (2010).
[doi:10.1103/PhysRevB.81.134510](https://doi.org/10.1103/PhysRevB.81.134510)
35. P. I. Bunyk, E. M. Hoskinson, M. W. Johnson, E. Tolkacheva, F. Altomare, A. J. Berkley, R. Harris, J. P. Hilton, T. Lanting, A. J. Przybysz, J. Whittaker, Architectural considerations in the design of a superconducting quantum annealing processor. *IEEE Trans. Appl. Supercond.* **24**, 1700110 (2014). [doi:10.1109/TASC.2014.2318294](https://doi.org/10.1109/TASC.2014.2318294)
36. J. D. Whittaker, L. J. Swenson, M. H. Volkmann, P. Spear, F. Altomare, A. J. Berkley, B. Bumble, P. Bunyk, P. K. Day, B. H. Eom, R. Harris, J. P. Hilton, E. Hoskinson, M. W. Johnson, A. Kleinsasser, E. Ladizinsky, T. Lanting, T. Oh, I. Perminov, E. Tolkacheva, J. Yao, A frequency and sensitivity tunable microresonator array for high-speed quantum processor readout. *J. Appl. Phys.* **119**, 014506 (2016). [doi:10.1063/1.4939161](https://doi.org/10.1063/1.4939161)
37. R. Harris, T. Lanting, A. J. Berkley, J. Johansson, M. W. Johnson, P. Bunyk, E. Ladizinsky, N. Ladizinsky, T. Oh, S. Han, Compound Josephson-junction coupler for flux qubits with minimal crosstalk. *Phys. Rev. B* **80**, 052506 (2009). [doi:10.1103/PhysRevB.80.052506](https://doi.org/10.1103/PhysRevB.80.052506)
38. V. Choi, Minor-embedding in adiabatic quantum computation: I. The parameter setting problem. *Quant. Inf. Proc.* **7**, 193–209 (2008). [doi:10.1007/s11128-008-0082-9](https://doi.org/10.1007/s11128-008-0082-9)
39. V. Choi, Minor-embedding in adiabatic quantum computation: II. Minor-universal graph design. *Quant. Inf. Proc.* **10**, 343–353 (2011). [doi:10.1007/s11128-010-0200-3](https://doi.org/10.1007/s11128-010-0200-3)
40. A. J. Berkley, A. J. Przybysz, T. Lanting, R. Harris, N. Dickson, F. Altomare, M. H. Amin, P. Bunyk, C. Enderud, E. Hoskinson, M. W. Johnson, E. Ladizinsky, R. Neufeld, C. Rich, A. Y. Smirnov, E. Tolkacheva, S. Uchaikin, A. B. Wilson, Tunneling spectroscopy using a probe qubit. *Phys. Rev. B* **87**, 020502 (2013). [doi:10.1103/PhysRevB.87.020502](https://doi.org/10.1103/PhysRevB.87.020502)
41. T. Lanting, A. J. Przybysz, A. Y. Smirnov, F. M. Spedalieri, M. H. Amin, A. J. Berkley, R. Harris, F. Altomare, S. Boixo, P. Bunyk, N. Dickson, C. Enderud, J. P. Hilton, E. Hoskinson, M. W. Johnson, E. Ladizinsky, N. Ladizinsky, R. Neufeld, T. Oh, I. Perminov, C. Rich, M. C. Thom, E. Tolkacheva, S. Uchaikin, A. B. Wilson, G. Rose, Entanglement in a quantum annealing processor. *Phys. Rev. X* **4**, 021041 (2014).
[doi:10.1103/PhysRevX.4.021041](https://doi.org/10.1103/PhysRevX.4.021041)
42. F. Yan, S. Gustavsson, A. Kamal, J. Birenbaum, A. P. Sears, D. Hover, T. J. Gudmundsen, D. Rosenberg, G. Samach, S. Weber, J. L. Yoder, T. P. Orlando, J. Clarke, A. J. Kerman, W. D. Oliver, The flux qubit revisited to enhance coherence and reproducibility. *Nat. Commun.* **7**, 12964 (2016). [doi:10.1038/ncomms12964](https://doi.org/10.1038/ncomms12964) [Medline](#)

43. T. W. B. Kibble, Topology of cosmic domains and strings. *J. Phys. Math. Gen.* **9**, 1387–1398 (1976). [doi:10.1088/0305-4470/9/8/029](https://doi.org/10.1088/0305-4470/9/8/029)
44. W. H. Zurek, Cosmological experiments in superfluid helium? *Nature* **317**, 505–508 (1985). [doi:10.1038/317505a0](https://doi.org/10.1038/317505a0)